

See discussions, stats, and author profiles for this publication at: <https://www.researchgate.net/publication/271592975>

Hydrothermal Continuous Flow Synthesis and Exfoliation of NiCo Layered Double Hydroxide Nanosheets for Enhanced Oxygen Evolution Catalysis

ARTICLE *in* NANO LETTERS · JANUARY 2015

Impact Factor: 13.59 · DOI: 10.1021/nl504872s · Source: PubMed

CITATIONS

17

READS

83

8 AUTHORS, INCLUDING:



[Hanfeng Liang](#)

Xiamen University

27 PUBLICATIONS 170 CITATIONS

[SEE PROFILE](#)



[Fei Meng](#)

Xiamen University

23 PUBLICATIONS 1,010 CITATIONS

[SEE PROFILE](#)



[Audrey Forticaux](#)

University of Wisconsin–Madison

9 PUBLICATIONS 580 CITATIONS

[SEE PROFILE](#)

Hydrothermal Continuous Flow Synthesis and Exfoliation of NiCo Layered Double Hydroxide Nanosheets for Enhanced Oxygen Evolution Catalysis

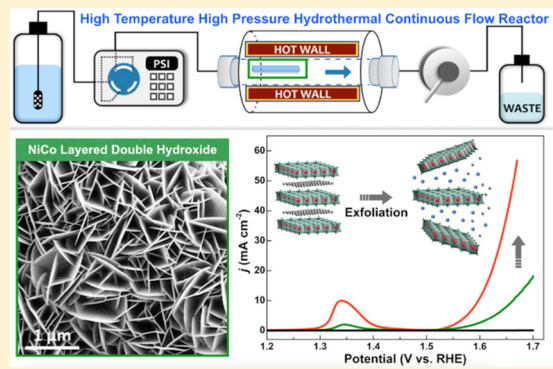
Hanfeng Liang,^{†,‡} Fei Meng,[†] Miguel Cabán-Acevedo,[†] Linsen Li,[†] Audrey Forticaux,[†] Lichen Xiu,[†] Zhoucheng Wang,[‡] and Song Jin^{*,†}

[†]Department of Chemistry, University of Wisconsin-Madison, 1101 University Ave., Madison, Wisconsin 53706, United States

[‡]College of Chemistry and Chemical Engineering, Xiamen University, Xiamen 361005, China

Supporting Information

ABSTRACT: We report the controlled synthesis of NiCo layered double hydroxide (LDH) nanoplates using a newly developed high temperature high pressure hydrothermal continuous flow reactor (HCFR), which enables direct growth onto conductive substrates in high yield and, most importantly, better control of the precursor supersaturation and, thus, nanostructure morphology and size. The solution coordination chemistry of metal–ammonia complexes was utilized to synthesize well-defined NiCo LDH nanoplates directly in a single step without topochemical oxidation. The as-grown NiCo LDH nanoplates exhibit a high catalytic activity toward the oxygen evolution reaction (OER). By chemically exfoliating LDH nanoplates to thinner nanosheets, the catalytic activity can be further enhanced to yield an electrocatalytic current density of 10 mA cm^{-2} at an overpotential of 367 mV and a Tafel slope of 40 mV dec^{-1} . Such enhancement could be due to the increased surface area and more exposed active sites. X-ray photoelectron spectroscopy (XPS) suggests the exfoliation also caused some changes in electronic structure. This work presents general strategies to controllably grow nanostructures of LDH and ternary oxide/hydroxides in general and to enhance the electrocatalytic performance of layered nanostructures by exfoliation.



KEYWORDS: Layered double hydroxide (LDH), hydrothermal continuous flow synthesis, nanoplates, exfoliation, nanosheets, oxygen evolution reaction (OER)

Layered double hydroxides (LDHs) are a family of synthetic two-dimensional (2D) layered materials that consist of stacked brucite-like $M^{II}(OH)_2$ layers, where some of the M^{II} ions are isomorphously substituted by M^{III} ions, giving positively charged host layers with charge-balancing anions between them (Figure 1A).^{1–3} The most studied LDHs can be described as $[M^{II}_{1-x}M^{III}_x(OH)_2]^{x+}(A^{n-})_{x/n}\cdot mH_2O$, where M^{II} (Mg, Fe, Ni, Cu, Zn, etc.) and M^{III} (Cr, Fe, Co, Al, Ga, etc.) are di- and trivalent metal cations, respectively, and A^{n-} is an anion (e.g., CO_3^{2-} , NO_3^- , ClO_4^-) that can be synthesized either by direct crystallization from aqueous solution or by anion exchange of a precrystallized LDH clay.^{1–3} Transition metal-based LDHs have found applications such as catalysis,^{2,3} photochemistry,^{3–5} drug delivery,⁶ and biotechnology,⁷ owing to their low cost, easily tailored properties, and versatility in compositions. Specifically, several classes of LDHs have been shown to act as efficient catalysts for oxygen evolution reaction (OER),^{8–13} and are inexpensive alternatives to the conventional precious metal-containing OER catalysts such as RuO_2 and IrO_2 . The versatile compositions of LDHs allow a wide selection of earth-abundant elements and endow them with unique catalytic properties when active components are suitably

located in the structure, making them particularly promising OER catalysts. However, most LDHs are prepared in the form of particle agglomerates and require additional binder-assisted film casting or coating procedures when evaluating them for OER,^{8–13} which suffers from the limited specific surface area and poor conductivity.

To improve their electrocatalytic performance, it is essential to prepare 2D LDH nanostructures with high surface area and well-defined morphology that are integrated with conductive substrates. The LDHs are usually synthesized by the conventional coprecipitation method in a closed-system under hydrothermal conditions,^{1,10–16} where precursors are added together at the beginning of the reaction all at once and allowed to react to completion. This approach suffers from a significant drop in precursor concentration (supersaturation) during the reaction,^{17,18} and such changes in the supersaturation lead to a convoluted and poorly controlled growth of the product. As a result, the LDHs produced by this method are usually big

Received: December 18, 2014

Revised: January 23, 2015



ACS Publications

© XXXX American Chemical Society

A

DOI: 10.1021/nl504872s
Nano Lett. XXXX, XXX, XXX–XXX

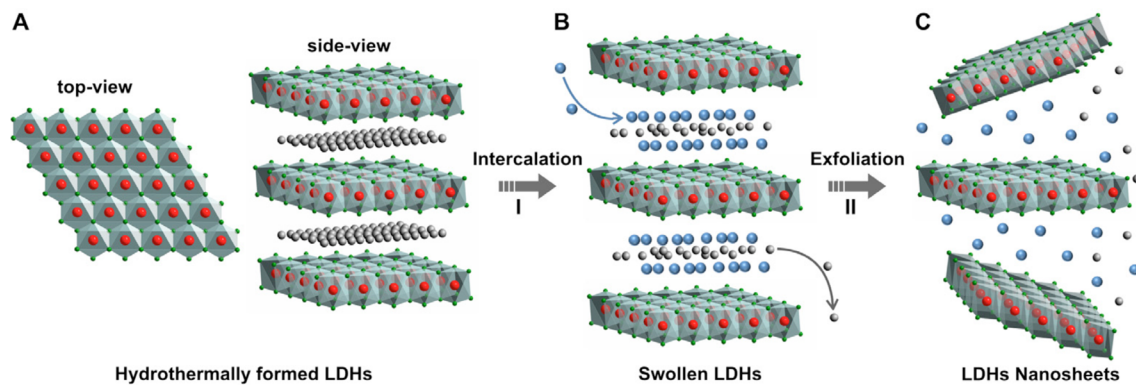


Figure 1. Schematic illustration of the crystal structure and the exfoliation process of LDHs. (A) Top-view and side-view of the LDHs crystal structure; (B) swollen LDHs with formamide molecules intercalated in the gallery; (C) exfoliated single layer nanosheets. Red spheres, metal atoms; green spheres, oxygen atoms; gray atoms, interlayer anions and water molecules; blue spheres, formamide molecules. Step I: the formamide molecules penetrate into the gallery by breaking the integrated hydrogen bonding network among the hydroxyl slabs, the interlayer anions and water molecules, producing a loosely stacked and highly swollen phase. Step II: the swollen LDHs are exfoliated into positively charged single layer nanosheets by stirring or mechanical shaking.

aggregated particles with a wide size distribution, which could limit their practical applications for OER and other catalysis. We have shown previously that nanoplates of 2D layered structures such as $\text{Ni}(\text{OH})_2$ and $\text{Co}(\text{OH})_2$ with well-defined morphology can be grown via the screw dislocation growth mechanism.¹⁹ Further, the key to improve the growth of dislocation-driven nanostructures is to control the precursor supersaturation at a constant low level, which can be achieved by continuously feeding precursors at low concentration into the reaction system.¹⁷ This strategy has been demonstrated for 1D nanowire and nanotube growth^{17,18,20,21} and should also help the growth of 2D nanostructures. Therefore, we set out to design a high temperature high pressure hydrothermal continuous flow reactor (HCFR) for the growth of LDHs. Compared with the continuous flow cells that operate at ambient conditions we developed previously,^{18,20,21} an important improvement is that this new HCFR can deliver and maintain a constant low supersaturation under *hydrothermal* conditions with *high pressure*. The more energetic reaction environment at high temperature and pressure can enhance the phase miscibility and precursor solubility and, thus, enable the formation of more complex compounds that are unattainable by low-temperature and low-pressure aqueous solution reactions.²² Furthermore, in hydrothermal conditions that are approaching the critical point of water, the solution viscosity is significantly reduced; thus, precursors can diffuse more readily (similarly to the high temperature vapor phase growth, but it can operate at a much lower temperature), which is beneficial to the growth of high quality crystals.

Moreover, the surface area of LDHs is also an important factor that affects their catalytic performance toward OER. The surface area of 2D LDH nanostructures can be further increased by swelling and exfoliating their layered structures into single layers with the assistance of polar organic solvents, such as formamide, that readily penetrate into the interlayer gallery and produce a loosely stacked and highly swollen LDH phase with increased spacings (Figure 1B).^{1,16,23,24} The formamide may also break the integrated hydrogen bonding network among the hydroxyl slabs, the interlayer anions, and water molecules and, hence, facilitates exfoliation (Figure 1C).^{1,16,23,24} Although the exfoliation of other layered materials for electrochemical applications (e.g., supercapacitors and electrocatalysis) has been demonstrated,^{25–30} the preparation

of nanosheets by exfoliation of bulk LDHs plates for OER¹¹ seems to be overlooked. We have previously shown that by chemical exfoliation, the catalytic activity of MoS_2 and WS_2 nanosheets for hydrogen evolution reaction could be significantly enhanced.^{28–30} Here, we extend this exfoliation concept to the LDHs to greatly increase their surface area, which could subsequently lead to a further enhanced catalytic activity toward OER.

In the present work, we chose NiCo LDH as a representative material to demonstrate our strategies: (1) using the HCFR to control the precursor supersaturation to achieve a better control over the nanostructure morphology and size and (2) further enhancing the catalytic activity by exfoliation. Although Ni- and Co-based materials by themselves have been considered as promising candidates for water splitting owing to their earth-abundance and theoretically high catalytic activities,^{31–35} the Ni and Co coexisting systems may further offer synergistic effect on the electrocatalysis.^{36,37} Therefore, it is expected that NiCo LDH would be a good catalyst for OER, even though it has rarely been studied, which may be partly due to the difficulty in controlling the oxidation states of the metal ions and the tedious synthetic procedures. Typically, the preparation of $\text{M}^{\text{II}}\text{Co}^{\text{III}}$ (M = divalent metal) LDHs requires three steps:^{11,14,16,38} the synthesis of $\text{M}^{\text{II}}\text{Co}^{\text{II}}$ mixed hydroxides by coprecipitation method (normally urea or hexamethylene-tetramine are used as precipitating agents), the subsequent oxidation of cobalt ions using iodine or bromine as topotactic oxidizer to get $\text{M}^{\text{II}}\text{Co}^{\text{III}}-\text{X}$ ($\text{X} = \text{I}^-$ or Br^-) LDH, and the intercalation of desired anions into the $\text{M}^{\text{II}}\text{Co}^{\text{III}}-\text{X}$ interlayers by anion exchange. The reason for these complex processes is that hydrated Co^{3+} ions are strong oxidants in aqueous solution and can even directly oxidize water; hence, an extra oxidation step is necessary to convert some of the Co^{2+} ions in the initially formed $\text{M}^{\text{II}}\text{Co}^{\text{II}}$ mixed hydroxides to $\text{M}^{\text{II}}\text{Co}^{\text{III}}$ LDHs. However, the $[\text{Co}^{\text{III}}(\text{NH}_3)_6]^{3+}$ complex (with a formation constant K_f of 4.6×10^{33}) is much more stable than $[\text{Co}^{\text{II}}(\text{NH}_3)_6]^{2+}$ ($K_f = 5.0 \times 10^4$), which means the initial Co^{2+} would be quickly oxidized to Co^{3+} by the dissolved oxygen in the solution so that we can synthesize NiCo LDH directly in one step without additional topochemical oxidation. Herein, we will demonstrate such direct synthesis in HCFR, which yields dense and uniform thin nanoplates of NiCo LDH grown directly on carbon paper support that can be readily

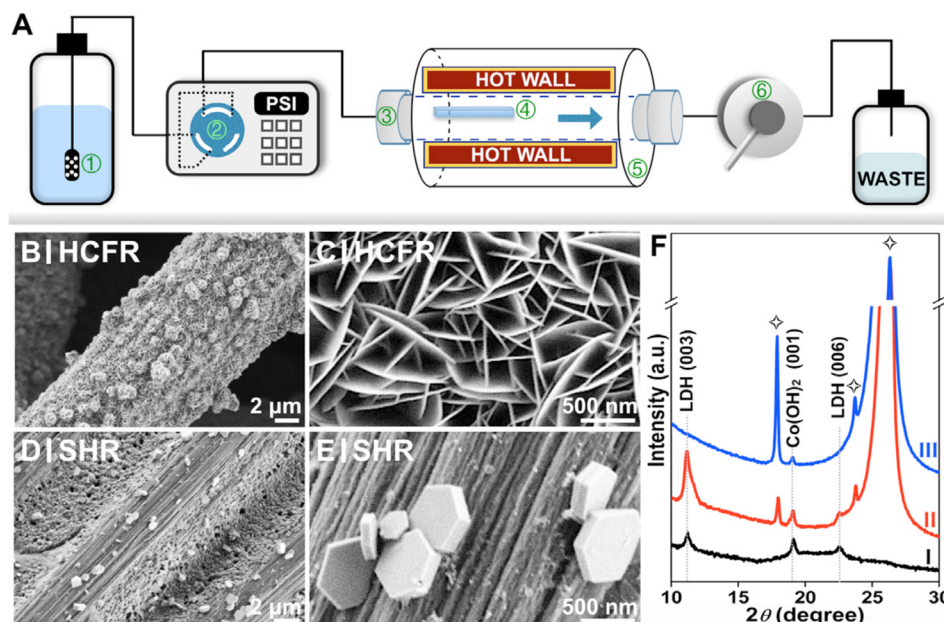


Figure 2. (A) Schematic of the HCFR (1. Reservoir; 2. HPLC pump; 3. Reaction column; 4. Substrate; 5. Tube furnace; and 6. Back pressure regulator). (B–E) SEM images of NiCo LDH nanostructures yielded from a HCFR reaction (B, C) and a SHR (D, E). (F) PXRD patterns of NiCo LDH powder collected from the HCFR reaction (I), NiCo LDH nanoplates on carbon paper yielded from a HCFR reaction (II) and a SHR (III). The stars mark the diffraction peaks from carbon paper substrate.

integrated into electrochemical water oxidation device with high catalytic activity toward OER. We also will show that exfoliation further enhances the catalytic activity dramatically.

We carried out the growth of NiCo LDH nanoplates on carbon paper using the HCFR we newly developed. As illustrated in Figure 2A, this system contains five major components: the precursor solution reservoir, a high performance liquid chromatography (HPLC) pump, a Teflon-lined 316 stainless-steel reaction column, a home-built tube furnace with temperature control, and a back pressure regulator (see the Supporting Information for more details). In commonly practiced static hydrothermal reactions (SHRs), the internal pressure of the reaction vessel is generated autonomously, that is, the evaporated solvent builds up the vapor pressure until the liquid–gas phase equilibrium is reached. In the new HCFR, we can use the back pressure regulator to adjust the internal pressure of the reaction system. In a typical synthesis, 2.4 mmol of $\text{Ni}(\text{NO}_3)_2 \cdot 6\text{H}_2\text{O}$ and 1.2 mmol of $\text{Co}(\text{NO}_3)_2 \cdot 6\text{H}_2\text{O}$ were dissolved in 352 mL of nanopure water, yielding a clear, light pink solution. After adding 48 mL of concentrated $\text{NH}_3 \cdot \text{H}_2\text{O}$ (28.0–30.0% NH_3 basis), the solution color turned dark brown, indicating the oxidation of Co^{2+} to Co^{3+} . This mixture was then continuously flowed through the HCFR heated at 160 °C at a speed of 1 mL min⁻¹ for 4 h. The reaction pressure was set to ~160 psi, which is slightly above the equilibrated vapor pressure of water at 160 °C (~102 psi), to ensure the reaction was carried out in liquidus environment. For comparison, we also performed a SHR employing the same precursor concentration and temperature conditions as those used for the HCFR reaction (see Supporting Information for experimental details). The scanning electron microscopy (SEM) images of the product made using HCFR (Figure 2B) clearly show nanoplates with high density are grown uniformly on the carbon paper support. These nanoplates with ~15 nm in thickness lie aslant or perpendicular to the substrate and are interconnected with each other, forming a highly open 3D

hierarchical structure (Figure 2C). In contrast, the SHR mainly yields thick nanoplates (~90 nm in thickness) as well as some small nanoparticles (Figures 2D and E). Moreover, the sparse nanoplates made by SHR are loosely deposited on the carbon paper without covering the whole surface. This distinct difference in product morphologies between HCFR reaction and SHR can also be observed for the products grown on other substrates, such as graphite disk and carbon cloth (Figure S1, Supporting Information). We also collected the free floating powder from the suspensions flowed through HCFR column, which shows the same thin nanoplate morphology as the product directly grown on carbon paper but more disordered and aggregated (see Figure S2 for SEM and TEM images, Supporting Information). This consistent contrast in product morphology and yield clearly shows that the HCFR enables better control over the morphology and the size of the product. We then performed powder X-ray diffraction (PXRD, Figure 2F) to identify the phase of the products. Except for the peaks originating from the carbon paper substrate, the diffraction peaks of the product made using HCFR (red curve) as well as those from the powder sample (black curve) collected from suspensions flowed through HCFR column, can be indexed to NiCo LDH along with a minor $\beta\text{-Co(OH)}_2$ phase. For the product made by SHR, although due to the lower product yield, no obvious LDH peaks are observed from the PXRD pattern (blue curve); the energy-dispersive X-ray spectroscopy (EDS) mapping (Figure S3, Supporting Information) clearly shows both Ni and Co elements are distributed uniformly in the nanoplates, suggesting the product is also NiCo LDH.

We then carried out the intercalation and exfoliation of the NiCo LDH nanoplates by immersing the carbon paper substrate covered with LDH nanoplates into formamide under the protection of N_2 gas (to avoid the formation of carbonate). For comparison, exfoliation was also performed on LDH nanplate powder sample that was collected from suspensions flowed through HCFR. For the powder sample,

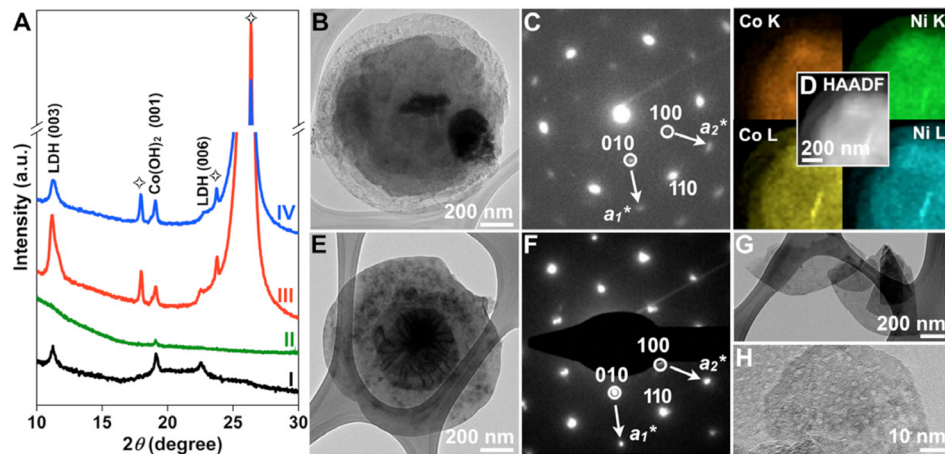


Figure 3. Structural characterizations of the NiCo LDH nanoplates (and nanosheets) before and after exfoliation. (A) XRD patterns of the various NiCo LDH nanostructures before and after exfoliation: (I, black curve) powder sample collected from suspensions flowed through HCFR; (II, green curve) powder sample after exfoliation; (III, red curve) as-synthesized nanoplates on carbon paper; (IV, blue curve) exfoliated nanosheets on carbon paper. The stars mark the diffraction peaks from carbon paper. (B) TEM image and (C) the corresponding SAED pattern of the as-synthesized NiCo LDH nanoplates on carbon paper grown via HCFR reaction. (D) The typical high-angle annular dark-field scanning TEM (HAADF-STEM) image of an individual nanoplate and the corresponding EDS mapping showing the distribution of Co and Ni elements. (E) TEM image and (F) the corresponding SAED pattern of the NiCo LDH after exfoliation. (G, H) Additional TEM images of the exfoliated thin nanosheet fragments from nanoplates grown on carbon paper (G) and from powder sample (H).

after being magnetically stirred for 48 h, a stable colloidal suspension of the LDH can be easily obtained. The presence of exfoliated nanosheets was first visually confirmed by the light scattering upon irradiation of the resulted suspension with a laser beam (Figure S4, Supporting Information). Further evidence of exfoliation comes from the XRD result (Figure 3A). The disappearance of the diffraction peaks associated with the stacking of the basal planes for the powder sample suggests that the host layers are no longer parallel.²³ For the nanoplates directly grown on carbon paper, although the basal plane peaks can still be observed after exfoliation, the intensity becomes much weaker. Note that the exfoliation procedures for nanoplates and powder sample are identical. Therefore, the decrease in the intensity of basal plane peaks observed indicates these nanoplates are partially exfoliated, which is reasonable because the nanoplates are attached to the carbon paper substrate, which may prevent them from being exfoliated as thoroughly as the free floating powder sample. Even though these nanoplates were partially exfoliated, they still showed some changes in morphology as revealed by SEM (Figure S5, Supporting Information) and transmission electron microscope (TEM) images. Figure 3B shows the typical TEM image of an original NiCo LDH nanoplate, which is light in contrast toward its periphery and darker in contrast in the center. The hexagonal spots in the selected area electron diffraction (SAED) pattern (Figure 3C) show that these two parts are of the same crystal phase and are single crystalline in nature. The lattice constant a (3.1 Å) measured from the SAED pattern (Figure 3C) is also consistent with reported NiCo LDH.¹⁴ The EDS elemental maps (Figure 3D) clearly show that the Ni and Co are homogeneously distributed in the nanoplates, confirming the as-prepared product is indeed NiCo LDH rather than separated Ni and Co hydroxides. After exfoliation, the darker part at the center of the nanoplate (Figure 3B) generally becomes much smaller (Figure 3E), whereas the SAED pattern (Figure 3F) confirms the crystal phase remains unchanged. Moreover, many thin nanosheets with irregular shapes, which may be caused by the severe

breakage or fracture of the original nanoplates during the exfoliation process, are also observed (Figure 3G). In comparison, TEM examination of the completely exfoliated powder sample reveals that those nanosheets are much smaller in size (Figure 3H). This result demonstrates that the exfoliation not only results in thinner layers but also reduces the size of the layers. Atomic force microscopy (AFM) was further performed to determine the height of the nanosheets (Figure S6, Supporting Information), which varies between ~0.6 nm and ~8.8 nm (the thickness of a single LDH layer is about 0.6 nm and the thickness of original nanoplates is ~15 nm), confirming that the NiCo LDH nanoplates are partially exfoliated.

We can conveniently evaluate the catalytic activity toward OER because high density NiCo LDH nanostructures are directly grown on the conductive carbon paper. The original NiCo LDH nanoplates and the exfoliated nanosheets were employed as working electrodes without using any extra binders (e.g., Nafion or polyvinylidene fluoride). The thick NiCo LDH nanoplates made by SHR and carbon paper were also tested as control samples. All electrochemical measurements were performed in O₂-saturated 1 M KOH solution in a standard three-electrode system (see details in Supporting Information). Figure 4A shows the iR -corrected (the serial resistances are generally smaller than 3 Ω for all samples) and background subtracted (see Figure S7, Supporting Information) polarization curves that were recorded at a low scan rate of 0.5 mV s⁻¹. The carbon paper substrate (I, black trace) has no measurable contribution to the observed catalytic activity for NiCo LDHs. The thick NiCo LDH nanoplates made by SHR (II, blue trace) also exhibits a relatively low OER activity, which could be due to the low mass loading, incomplete coverage, and small surface area. In contrast, the thin NiCo LDH nanoplates with high density made using HCFR (III, green trace) shows a higher catalytic activity in terms of lower onset overpotential and larger catalytic current density (j). Note that the peaks around 1.34 V can be assigned to the oxidation of M(II) to M(III or IV) (M = Ni and Co).³⁹ The NiCo LDH nanoplates

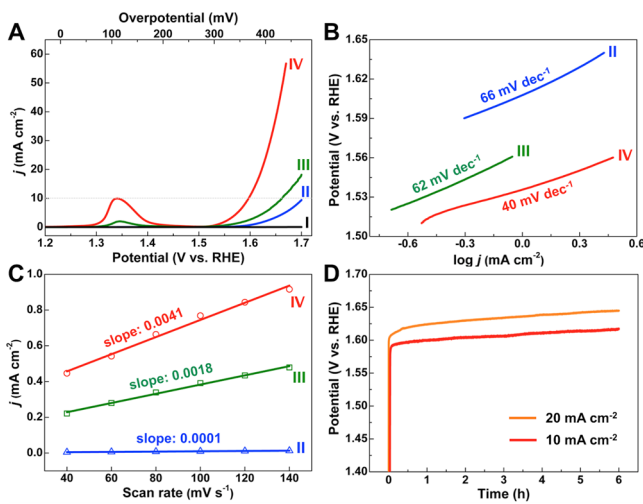


Figure 4. Electrochemical properties of various forms of NiCo LDH nanostructures for OER. (A) iR -corrected and background subtracted polarization curves of NiCo LDH catalysts and carbon paper in O_2 -saturated 1 M KOH at a scan rate of 0.5 mV s^{-1} and (B) the corresponding Tafel plots. (C) Differences in current density ($j_a - j_c$) at 0.2 V vs SCE plotted against scan rate fitted to a linear regression allows for the estimation of electrochemical double layer capacitance. (D) Long-term stability test of exfoliated NiCo LDH nanosheets carried out under constant current densities of 10 mA cm^{-2} (red curve) and 20 mA cm^{-2} (orange curve). Samples: (I) carbon paper; (II) NiCo LDH nanoplates made by SHR, catalyst loading $\sim 0.08\text{ mg cm}^{-2}$; (III) NiCo LDH nanoplates made using HCFR, catalyst loading $\sim 0.23\text{ mg cm}^{-2}$; (IV) NiCo LDH nanosheets exfoliated from HCFR synthesized nanoplates, catalyst loading $\sim 0.17\text{ mg cm}^{-2}$.

grown on different substrates show comparable OER performance (Figure S8, Supporting Information). Here, we like to emphasize that compared with powder sample, which needs extra binders to fabricate electrodes, the well-defined nanoplate arrays with a highly open structure directly grown on carbon paper using HCFR facilitates the diffusion of ionic species and enables efficient utilization of active sites (which are not being

blocked by binders). Perhaps not surprisingly, these thin nanoplates made using HCFR show a better performance for OER than the powder sample collected from the same HCFR reaction (Figure S9, Supporting Information). Moreover, the direct electrical contact of the nanoplates with carbon paper, which served as the current collector in this case, ensures good conductivity between them. These intrinsic advantages make the integrated nanoplate arrays more attractive than powder sample for OER.

Furthermore, the catalytic activity of LDH nanostructures can be significantly enhanced by the exfoliation treatment, as shown by an even lower onset overpotential and higher current density for the OER (Figure 4A, IV, red trace). Specifically, the exfoliated NiCo LDH nanosheets require an applied overpotential as low as 367 mV vs the reversible hydrogen electrode (RHE) to achieve significant O_2 evolution ($j = 10\text{ mA cm}^{-2}$), whereas the original nanoplates and the thick nanoplates made by SHR require 430 and 474 mV vs RHE, respectively. Note that the exfoliated sample (IV) with enhanced catalytic performance even has a lower mass loading ($\sim 0.17\text{ mg cm}^{-2}$) than the original sample (III, $\sim 0.23\text{ mg cm}^{-2}$) before exfoliation. We then fitted the polarization curves to the Tafel equation and the plots are shown in Figure 4B. Evidently, the exfoliated nanosheets exhibit a lower Tafel slope of 40 mV dec^{-1} than the original nanoplates made using HCFR (62 mV dec^{-1}), which is similar to that of the thick nanoplates made by SHR (66 mV dec^{-1}). This suggests the reaction kinetics for exfoliated LDH nanosheets is more favorable than the bulk NiCo LDH samples and there is change in the intrinsic catalytic activity.

We also estimated the double-layer capacitances (C_{dl}) of the NiCo LDHs by using a simple cyclic voltammetry (CV) method,⁴⁰ in order to compare the electrochemically active surface areas (ECSA) of the various NiCo LDH samples, because the C_{dl} is linearly proportional to the ECSA. Figure 4C shows the plots of $\Delta j = j_a - j_c$ at 0.2 V vs saturated calomel electrode against the scan rates. Apparently, the slope (equivalent to twice the C_{dl}) of the exfoliated nanosheets is much higher than the LDH nanoplates, which reveals that they

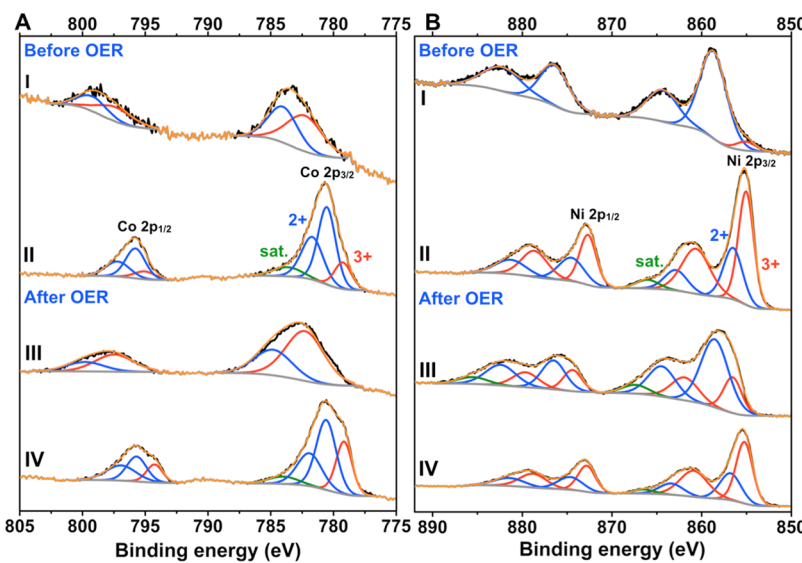


Figure 5. High resolution XPS spectra for Co 2p (A) and Ni 2p (B) and peak fitting analysis of the original NiCo LDH nanoplates made using HCFR (I, before OER scan; III, after OER scan) and exfoliated nanosheets (II, before OER scan; IV, after OER scan). Black lines, raw data; red, blue and green lines, fit components; orange lines, fit sum curves; gray lines, backgrounds.

have the largest active surface area. It is interesting that from the thick nanoplates made by SHR to the nanoplates made using HCFR, the ECSA increases by 18-fold while the OER performance (in terms of the current density at 400 mV) becomes twice as large. However, from the nanoplates made using HCFR to the exfoliated nanosheets, there was a 2-fold increase in ECSA but a 7-fold increase in the OER performance. This comparison implies that the increase in ECSA upon the exfoliation is not the only important factor that leads to the enhanced catalytic performance, which is consistent with the comparison of Tafel slopes discussed above. There is some analogy to the exfoliated metallic MoS₂ and WS₂ nanosheets for hydrogen evolution catalysis, where the enhancement in catalytic activity cannot be fully accounted for by the increase in ECSA and the Tafel slope was also significantly reduced.^{28,29} It is worth mentioning that the exfoliation could also reduce the size of the layers as shown by TEM and AFM imaging as discussed above. This reduction would lead to an increase in the number of edge sites thus benefit the catalytic activity because the open coordination sites located along the edges may be more active for OER.¹¹ In fact, an increase in the area of the anodic peak around 1.34 V associated with the oxidation of Ni(II)/Co(II) is observed after exfoliation (Figure 4A), suggesting the exfoliation also makes more active sites accessible. Furthermore, the exfoliated nanosheets exhibited a good stability under continuous operation in alkaline solution. An initial operating potential of 1.593 V was required to deliver a current density of 10 mA cm⁻² (Figure 4D). After 6 h, the required potential only slightly increased to 1.615 V. The early onset of significant oxygen evolution, small Tafel slope, and good durability confirm that the exfoliated NiCo LDH nanosheets is a highly active OER catalyst that is at least comparable to the best reported OER catalysts^{41–44} (see comparison in Table S1, Supporting Information).

We further carried out X-ray photoelectron spectroscopy (XPS) measurements on the as-grown and exfoliated LDH nanostructures before and after OER measurements to probe their surface compositions and chemical states. It should be mentioned that it was reported that even trace amount of iron impurity that possibly comes from the KOH electrolyte could also contribute to the OER performance of the metal (oxy)hydroxides,⁴⁵ even though we did not observe any detectable iron from XPS (Figure S10, Supporting Information). The Co 2p (Figure 5A-I) and Ni 2p (Figure 5B-I) spectra of the as-synthesized nanoplates are split into 2p_{3/2} and 2p_{1/2} doublets due to spin-orbit coupling. Peak fitting analysis of Co 2p for the as-synthesized nanoplates shows two distinct cobalt species, which can be identified as Co²⁺ (2p_{3/2} peak at 784.15 eV) and Co³⁺ (2p_{3/2} peak at 782.33 eV). After OER measurements the relative intensity for Co³⁺ increases (Figure 5A-III), which provides supporting evidence for the chemical identity of Co 2p species. The observation of both Co²⁺ and Co³⁺ species for the as-synthesized nanoplates (Figure 5A-I) further confirms the efficacy of using [Co^{III}(NH₃)₆]³⁺ complex to directly synthesize NiCo LDH. Whereas the peak fitting analysis of Ni 2p indicates predominantly Ni²⁺ (2p_{3/2} peak at 858.86 eV) for the as-synthesized nanoplates, however, similarly to Co 2p there is an increase in Ni³⁺ species (2p_{3/2} peak at 855.05 eV, Figure 5B-III) after OER measurements. These observed binding energies for Co 2p and Ni 2p peaks are a little different from those reported for NiCo oxide⁴⁶ or NiCo LDH,¹⁶ which could be due to the different composition of our

sample. After exfoliation of the nanoplates, a significant shift (~3 eV) to lower binding energy for Co 2p (Figure 5A-II) and Ni 2p (Figure 5B-II) doublets is observed, indicating a change in the electronic structure of the exfoliated NiCo LDH. The peak fitting analysis of Co 2p (Figure 5A-II) shows that the chemical species of Co can be identified as Co²⁺ (780.5 and 781.9 eV) and Co³⁺ (779.2 eV), and their binding energies are close to those reported for Co(OH)₂,⁴⁷ and Co₃O₄,⁴³ respectively. Peak fitting analysis of Co 2p and Ni 2p after exfoliation also shows a significant change in the relative ratio of M²⁺/M³⁺ (M = Ni, Co) chemical species, which could be connected to the observed binding energy shift. Such changes in electronic structure could be due to the changing interactions between LDH layers and intercalants before and after exfoliation. Note that for the MS₂ (M = Mo and W), chemical exfoliation causes an important phase transition from the original semiconducting 2H-MX₂ to metallic 1T-MX₂, which is the main reason for their enhanced catalytic hydrogen evolution activity.^{28,29} Though in this case, the XPS experiments suggest that the oxidation states and electronic structures of NiCo LDH are quite complex and dynamic upon both exfoliation and OER measurements. How these are impacted by interlayer interaction and how they influence the catalytic activity are not well understood and further studies (and possibly theoretical analysis) are needed.

In summary, we report the controlled solution synthesis of NiCo LDH nanoplates by using ammonia and metal salts as feeding precursors in a newly developed HCFR. The facile oxidation of initially formed [Co^{II}(NH₃)₆]²⁺ to [Co^{III}(NH₃)₆]³⁺ ensures the effective incorporation of Co(III) species into NiCo LDH product in a direct one-step synthesis. The HCFR utilized here can maintain the precursor concentration (supersaturation) at a constant level in hydrothermal reactions thus enables a better control over the morphology and size of the product. As a result, we were able to directly grow thin NiCo LDH nanoplates with high density on carbon paper, which can be directly used for OER with high performance. Furthermore, their catalytic activity can be significantly enhanced by liquid-phase exfoliation into NiCo LDH nanosheets. Structural characterization showed that the exfoliation not only resulted in thinner layers with reduced size but also caused a change in the electronic structure. This work demonstrates the importance of controlling the supersaturation for growing LDH nanoplates and opens up opportunities for rational design and solution growth of 2D layered materials with well-defined morphology in general.^{48,49} Our work also suggests a general strategy to enhance the electrocatalytic performance of layered materials by chemical exfoliation.

■ ASSOCIATED CONTENT

■ Supporting Information

Details of method, additional SEM and TEM images of other samples, photograph of emulsion of exfoliated sample, AFM topographical images of exfoliated nanosheets, polarization curves showing background corrections, comparison of catalytic performance, and XPS survey spectra. This material is available free of charge via the Internet at <http://pubs.acs.org>.

■ AUTHOR INFORMATION

Corresponding Author

*E-mail: jin@chem.wisc.edu.

Notes

The authors declare no competing financial interest.

ACKNOWLEDGMENTS

This research is supported by NSF Grant DMR-1106184. S.J. also thanks the Research Corporation SciaLog Award and UW—Madison H. I. Romnes Faculty Fellowship for support. H.L. thanks the China Scholarship Council for support. M.C.-A. thanks the NSF Graduate Research Fellowship for support. Z.W. thanks the National Natural Science Foundation of China (grant no. 51372212) for support.

REFERENCES

- (1) Wang, Q.; O'Hare, D. *Chem. Rev.* **2012**, *112*, 4124–4155.
- (2) Fan, G.; Li, F.; Evans, D. G.; Duan, X. *Chem. Soc. Rev.* **2014**, *43*, 7040–7066.
- (3) Li, F.; Duan, X. *Struct. Bonding (Berlin, Ger.)* **2006**, *119*, 193–223.
- (4) Cho, S.; Jang, J. W.; Park, Y. B.; Kim, J. Y.; Magesh, G.; Kim, J. H.; Seol, M.; Yong, K.; Lee, K. H.; Lee, J. S. *Energy Environ. Sci.* **2014**, *7*, 2301–2307.
- (5) Zhao, Y.; Li, B.; Wang, Q.; Gao, W.; Wang, C. J.; Wei, M.; Evans, D. G.; Duan, X.; O'Hare, D. *Chem. Sci.* **2014**, *5*, 951–958.
- (6) Li, L.; Gu, W.; Chen, J.; Chen, W.; Xu, Z. P. *Biomaterials* **2014**, *35*, 3331–3339.
- (7) Shao, M.; Ning, F.; Zhao, J.; Wei, M.; Evans, D. G.; Duan, X. *J. Am. Chem. Soc.* **2012**, *134*, 1071–1077.
- (8) Chen, S.; Duan, J.; Jaroniec, M.; Qiao, S. Z. *Angew. Chem., Int. Ed.* **2013**, *52*, 13567–13570.
- (9) Gong, M.; Li, Y.; Wang, H.; Liang, Y.; Wu, J. Z.; Zhou, J.; Wang, J.; Regier, T.; Wei, F.; Dai, H. *J. Am. Chem. Soc.* **2013**, *135*, 8452–8455.
- (10) Song, F.; Hu, X. *J. Am. Chem. Soc.* **2014**, *136*, 16481–16484.
- (11) Song, F.; Hu, X. *Nat. Commun.* **2014**, *5*, 4477.
- (12) Zou, X.; Goswami, A.; Asefa, T. *J. Am. Chem. Soc.* **2013**, *135*, 17242–17245.
- (13) Oliver-Tolentino, M. A.; Vázquez-Samperio, J.; Manzo-Robledo, A.; González-Huerta, R. D. G.; Flores-Moreno, J. L.; Ramírez-Rosales, D.; Guzmán-Vargas, A. *J. Phys. Chem. C* **2014**, *118*, 22432–22438.
- (14) Zhang, Y.; Cui, B.; Zhao, C.; Lin, H.; Li, J. *Phys. Chem. Chem. Phys.* **2013**, *15*, 7363–7369.
- (15) Liu, Z.; Ma, R.; Osada, M.; Iyi, N.; Ebina, Y.; Takada, K.; Sasaki, T. *J. Am. Chem. Soc.* **2006**, *128*, 4872–4880.
- (16) Liang, J.; Ma, R.; Iyi, N.; Ebina, Y.; Takada, K.; Sasaki, T. *Chem. Mater.* **2010**, *22*, 371–378.
- (17) Meng, F.; Morin, S. A.; Forticaux, A.; Jin, S. *Acc. Chem. Res.* **2013**, *46*, 1616–1626.
- (18) Morin, S. A.; Bierman, M. J.; Tong, J.; Jin, S. *Science* **2010**, *328*, 476–480.
- (19) Morin, S. A.; Forticaux, A.; Bierman, M. J.; Jin, S. *Nano Lett.* **2011**, *11*, 4449–4455.
- (20) Meng, F.; Morin, S. A.; Jin, S. *J. Am. Chem. Soc.* **2011**, *133*, 8408–8411.
- (21) Meng, F.; Jin, S. *Nano Lett.* **2012**, *12*, 234–239.
- (22) Modeshia, D. R.; Walton, R. I. *Chem. Soc. Rev.* **2010**, *39*, 4303–4325.
- (23) Ma, R.; Liu, Z.; Li, L.; Iyi, N.; Sasaki, T. *J. Mater. Chem.* **2006**, *16*, 3809–3813.
- (24) Liu, Z.; Ma, R.; Ebina, Y.; Iyi, N.; Takada, K.; Sasaki, T. *Langmuir* **2007**, *23*, 861–867.
- (25) Yu, L.; Yan, Y. X.; Liu, Q.; Wang, J.; Yang, B.; Wang, B.; Jing, X. Y.; Liu, L. H. *J. Electrochem. Soc.* **2014**, *161*, E1–E5.
- (26) Wang, H.; Lu, Z.; Xu, S.; Kong, D.; Cha, J. J.; Zheng, G.; Hsu, P.-C.; Yan, K.; Bradshaw, D.; Prinz, F. B.; Cui, Y. *Proc. Natl. Acad. Sci. U.S.A.* **2013**, *110*, 19701–19706.
- (27) Voiry, D.; Yamaguchi, H.; Li, J.; Silva, R.; Alves, D. C. B.; Fujita, T.; Chen, M.; Asefa, T.; Shenoy, V. B.; Eda, G.; Chhowalla, M. *Nat. Mater.* **2013**, *12*, 850–855.
- (28) Lukowski, M. A.; Daniel, A. S.; Meng, F.; Forticaux, A.; Li, L.; Jin, S. *J. Am. Chem. Soc.* **2013**, *135*, 10274–10277.
- (29) Lukowski, M. A.; Daniel, A. S.; English, C. R.; Meng, F.; Forticaux, A.; Hamers, R. J.; Jin, S. *Energy Environ. Sci.* **2014**, *7*, 2608–2613.
- (30) Ding, Q.; Meng, F.; English, C. R.; Cabán-Acevedo, M.; Shearer, M. J.; Liang, D.; Daniel, A. S.; Hamers, R. J.; Jin, S. *J. Am. Chem. Soc.* **2014**, *136*, 8504–8507.
- (31) Subbaraman, R.; Tripkovic, D.; Chang, K.-C.; Strmcnik, D.; Paulikas, A. P.; Hirunsit, P.; Chan, M.; Greeley, J.; Stamenkovic, V.; Markovic, N. M. *Nat. Mater.* **2012**, *11*, 550–557.
- (32) Kanan, M. W.; Nocera, D. G. *Science* **2008**, *321*, 1072–1075.
- (33) Ma, T. Y.; Dai, S.; Jaroniec, M.; Qiao, S. Z. *J. Am. Chem. Soc.* **2014**, *136*, 13925–13931.
- (34) Gao, M.; Sheng, W.; Zhuang, Z.; Fang, Q.; Gu, S.; Jiang, J.; Yan, Y. *J. Am. Chem. Soc.* **2014**, *136*, 7077–7084.
- (35) Faber, M. S.; Jin, S. *Energy Environ. Sci.* **2014**, *7*, 3519–3542.
- (36) Li, Y.; Hasin, P.; Wu, Y. *Adv. Mater.* **2010**, *22*, 1926–1929.
- (37) Liu, X.; Shi, S.; Xiong, Q.; Li, L.; Zhang, Y.; Tang, H.; Gu, C.; Wang, X.; Tu, J. *ACS Appl. Mater. Interfaces* **2013**, *5*, 8790–8795.
- (38) Ma, R.; Takada, K.; Fukuda, K.; Iyi, N.; Bando, Y.; Sasaki, T. *Angew. Chem., Int. Ed.* **2008**, *47*, 86–89.
- (39) Salunkhe, R. R.; Jang, K.; Lee, S.; Ahn, H. *RSC Adv.* **2012**, *2*, 3190–3193.
- (40) Faber, M. S.; Dziedzic, R.; Lukowski, M. A.; Kaiser, N. S.; Ding, Q.; Jin, S. *J. Am. Chem. Soc.* **2014**, *136*, 10053–10061.
- (41) McCrory, C. C. L.; Jung, S.; Peters, J. C.; Jaramillo, T. F. *J. Am. Chem. Soc.* **2013**, *135*, 16977–16987.
- (42) Ma, T. Y.; Ran, J.; Dai, S.; Jaroniec, M.; Qiao, S. Z. *Angew. Chem., Int. Ed.* **2015**, DOI: 10.1002/anie.201411125.
- (43) Ma, T. Y.; Dai, S.; Jaroniec, M.; Qiao, S. Z. *Angew. Chem., Int. Ed.* **2014**, *53*, 7281–7285.
- (44) Chen, S.; Duan, J.; Jaroniec, M.; Qiao, S. Z. *Adv. Mater.* **2014**, *26*, 2925–2930.
- (45) Trotocaud, L.; Young, S. L.; Ranney, J. K.; Boettcher, S. W. *J. Am. Chem. Soc.* **2014**, *136*, 6744–6753.
- (46) Yuan, C.; Li, J.; Hou, L.; Zhang, X.; Shen, L.; Lou, X. W. *Adv. Funct. Mater.* **2012**, *22*, 4592–4597.
- (47) Biesinger, M. C.; Payne, B. P.; Grosvenor, A. P.; Lau, L. W. M.; Gerson, A. R.; Smart, R. S. C. *Appl. Surf. Sci.* **2011**, *257*, 2717–2730.
- (48) Zhuang, A.; Li, J. J.; Wang, Y. C.; Wen, X.; Lin, Y.; Xiang, B.; Wang, X.; Zeng, J. *Angew. Chem., Int. Ed.* **2014**, *126*, 6543–6547.
- (49) Kort, K. R.; Banerjee, S. *Small* **2015**, *11*, 329–334.

Hydrothermal Continuous Flow Synthesis and Exfoliation of NiCo Layered Double Hydroxide Nanosheets for Enhanced Oxygen Evolution Catalysis

Hanfeng Liang,^{†‡} Fei Meng,[†] Miguel Cabán-Acevedo,[†] Linsen Li,[†] Audrey Forticaux,[†] Lichen Xiu,[†] Zhoucheng Wang,[‡] and Song Jin^{†,}*

[†]Department of Chemistry, University of Wisconsin-Madison, 1101 University Ave., Madison, Wisconsin 53706, United States and [‡]College of Chemistry and Chemical Engineering, Xiamen University, Xiamen 361005, China.

I. Experimental Details

I.1. High temperature high pressure hydrothermal continuous flow reactor (HCFR) setup

The HCFR contains five major components (Figure 1): the precursor solution reservoir, a high performance liquid chromatography (HPLC) pump (Shimazu[®], LC-20AD), a Teflon-lined 316 stainless steel reaction column (HPLC preparative column, Higgins Clipeus[®], 250 mm length, 20 mm I. D. without the Teflon liner and 13 mm I.D. with the Teflon liner, the packing material has been removed), a home-built tube furnace (Omega[®], CRW S-62/60-A) with temperature control (Dwyer[®], 16C-2, RS-485 communication), and a back pressure regulator (Swagelok[®], KBP1J0A4C5A20000 for pressure below 500 psi, and KPB1S0A425P20000 for pressure between 500 to 4000 psi). They are connected by 316 stainless steel HPLC tubing (Sigma-Aldrich[®], 1/16 in O. D., 0.040 in I. D.).

Before each reaction, the system is cleaned by continuously flushing with nanopure water (Thermo Scientific, Banstead Nanopure, 18.2 MΩ cm). The reaction column is preloaded with the substrate (such as carbon paper or graphite disks) mounted facing down and the precursor

solution approximately to its maximum volume (~30 mL), and sealed with stainless steel caps. Then the reaction column is placed through the tube furnace and connected with the HPLC pump and the back pressure regulator. Next a leakage test is performed: first the HPLC pump is turned on to inject the precursor solution through the column reactor; then by adjusting the back pressure regulator, the internal pressure reading of the system shown on the control panel of the HPLC pump should be gradually elevated, which is the indication of no leakage. All of the connection junctions are also carefully examined with a piece of dry Kimwipe paper. After no leakage is confirmed, the regulator is set to the desired pressure, and the furnace is turned on to heat the reaction solution to the set temperature to start the reaction at a certain flow rate. The reaction is stopped by turning off the HPLC pump and the tube furnace, while an air flow is used to cool down the reaction column. Finally the pressure is released by completely opening the valve of back pressure regulator and the column can be uninstalled to collect the products on the substrates mounted inside. The products in the solution/suspension that us flowed through the HCFR can also be collected.

Note that although here we named this home-built flow reactor as “HCFR”, it is also capable of running solvothermal flow reactions when non-aqueous solvents are used instead of water.

I.2. Synthesis and exfoliation of NiCo layered double hydroxide (LDH)

Reagents. Nickel(II) nitrate hexahydrate ($\text{Ni}(\text{NO}_3)_2 \cdot 6\text{H}_2\text{O}$, CAS# 13478-00-7), cobalt(II) nitrate hexahydrate ($\text{Co}(\text{NO}_3)_2 \cdot 6\text{H}_2\text{O}$, ≥98%, CAS# 10026-22-9), ammonium hydroxide solution ($\text{NH}_3 \cdot \text{H}_2\text{O}$, 28.0-30.0% NH_3 basis, CAS# 1336-21-6) and formamide (HCONH_2 , 99.5%, CAS# 75-12-7) were purchased from Sigma Aldrich and used as received.

1.2.1. Synthesis using the HCFR

Precursor solution preparation. 0.7 g (2.4 mmol) of $\text{Ni}(\text{NO}_3)_2 \cdot 6\text{H}_2\text{O}$, 0.35 g (1.2 mmol) of $\text{Co}(\text{NO}_3)_2 \cdot 6\text{H}_2\text{O}$ were dissolved in 352 mL of nanopure water (18.2 MΩ cm), yielding a clear, light pink solution. Then 48 mL of concentrated $\text{NH}_3 \cdot \text{H}_2\text{O}$ was added to the above solution, which resulted in a color change from light pink to brown dark, indicating the Co(II) was oxidized to Co(III) by dissolved oxygen (at least partially).^{s1} This mixture was then used as the feeding precursor solution in the reservoir for continuous flow reaction.

Substrate preparation. 5% Teflon treated carbon paper (FuelCellEarth, TGP-H-060) with 10 cm in length and 1 cm in width was attached onto a glass sheet with approximately 13 mm in width using adhesive carbon tape. Then the substrate was pushed into the center of the HCFR column before the precursor solution was loaded and the column was sealed.

Hydrothermal continuous flow reaction. The reaction column with preloaded precursor solution (~30 mL) was placed through the tube furnace and connected with the HPLC pump and the back pressure regulator. Then the furnace was turned on to heat the reaction solution to 160 °C (~10 min) and kept at that temperature for another ~20 min to allow the seed growth before the feeding precursor solution was flowed at a speed of 1.0 mL min⁻¹. The pressure was set to ~160 psi and would stay constant throughout the reaction if there is no leakage or clogging. After 4 h reaction, the heating and the flow were stopped and an air flow was used to cool down the reaction column. Finally the pressure was released by completely opening the valve of back pressure regulator and the column could be uninstalled. The substrate (carbon paper) was then removed from the column, rinsed with nanopure water and ethanol, and dried in a flow of N₂ gas. The mass loading of the catalyst was determined by weighting the carbon paper substrate before and after reaction.

I.2.2. Static hydrothermal synthesis

The static hydrothermal reaction employed the same precursor concentration and temperature conditions as those in a HCFR reaction. Typically, 60 mL of the precursor solution was transferred into a Teflon-lined stainless steel autoclave with a capacity of 80 mL. A piece of carbon paper (8 cm × 1 cm) attached onto a glass sheet was then immersed into the solution. The autoclave was sealed and heated at 160 °C for 4 h. After the reaction, the substrate was rinsed with nanopure water and ethanol, and then dried in a flow of N₂ gas.

I.2.3. Exfoliation of LDH by formamide

For the exfoliation of the as-prepared LDH, the carbon paper substrate (1 cm × 4 cm) with NiCo LDH nanoplates grown on it or the LDH powder (5 mg) was immersed in 150 mL of formamide in a flask. The flask was tightly sealed after purging with N₂ gas and then agitated under magnetic stirring for 48 h.

I.3. Structural characterization

Powder X-ray diffraction (PXRD) measurements were performed on a Bruker D8 Advance powder X-ray diffractometer using Cu K α radiations. For scanning electron microscopy (SEM), samples were imaged using a LEO Supra 55 VP field emission SEM. For transmission electron microscopy (TEM) observation, the NiCo LDH nanoplates grown on carbon paper were immersed into ethanol and sonicated for 5 min. Then a few drops of the suspension were casted onto lacey carbon supported TEM grids. TEM was carried out on a FEI Titan transmission electron microscope operated at an accelerating voltage of 200 kV. Energy-dispersive X-ray spectroscopy (EDS) elemental mapping was performed on the same instrument in scanning TEM (STEM) mode. Atomic force microscopy (AFM) images were recorded using a Digital Instrument Multi-Mode AFM with a Nanoscope 4 controller operating in tapping mode.

I.4. Electrochemical characterization

Electrochemical measurements were performed using a three-electrode cell connected to a Bio-Logic SP-200 potentiostat. All measurements were performed in O₂-saturated 1 M KOH solution (pH = 13.6), using the NiCo LDH nanoplates on carbon paper or other samples as the working electrode, a Pt wire as the counter electrode, and a saturated calomel (SCE) reference electrode. The potentials in this work were referenced to the reversible hydrogen electrode (RHE) according to the Nernst equation, and in 1 M KOH, $E(\text{RHE}) = E(\text{SCE}) + 1.0464 \text{ V}$. Linear sweep voltammograms (LSV) were measured from 1.2 V to 1.8 V versus RHE at a scan rate of 0.5 mV s⁻¹. Electrochemical impedance spectroscopy (EIS) was performed at open circuit potential over a frequency range from 10 mHz to 5 MHz with a 10 mV AC dither. Chronopotentiometric measurements were recorded at current densities of 10 and 20 mA cm⁻². All experiments were conducted at room temperature (25 °C).

II. Supporting Figures and Table

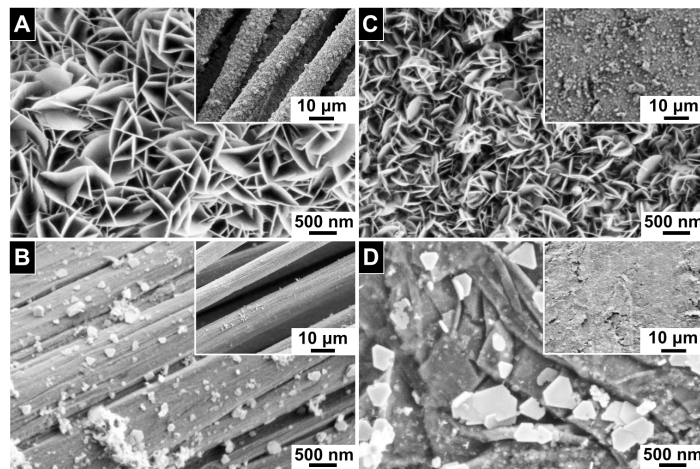


Figure S1. Comparison of the NiCo LDH nanostructures made by hydrothermal continuous flow reactor (HCFR) reaction and static hydrothermal reaction (SHR). (A, B) SEM images of NiCo LDH nanostructures on carbon cloth yielded from a HCFR reaction (A) and a SHR (B). (C, D) SEM images of NiCo LDH nanostructures on graphite disk yielded from a HCFR (C) and a SHR (D).

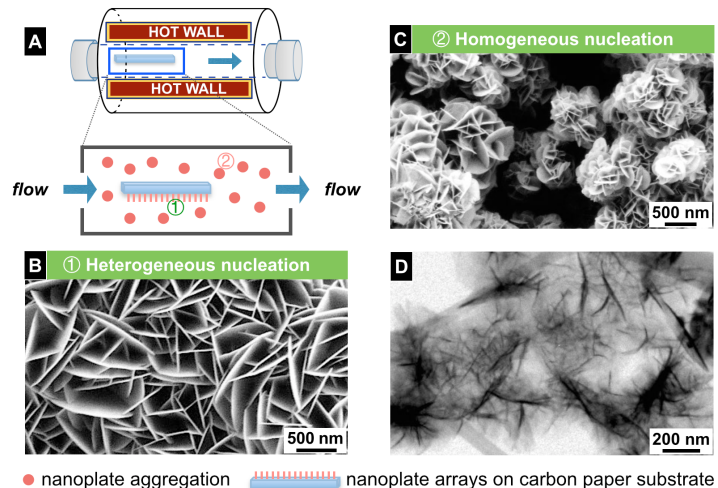


Figure S2. (A) Schematic diagram for the different formation processes of particles grown in solution (homogeneous nucleation) and on carbon paper substrate (heterogeneous nucleation). (B) SEM image of the NiCo LDH nanoplate arrays grown on carbon paper via heterogeneous nucleation mechanism. (C) SEM and (D) TEM images of the free floating powder sample grown

via homogeneous nucleation mechanism collected from the solution in HCFR column after reaction.

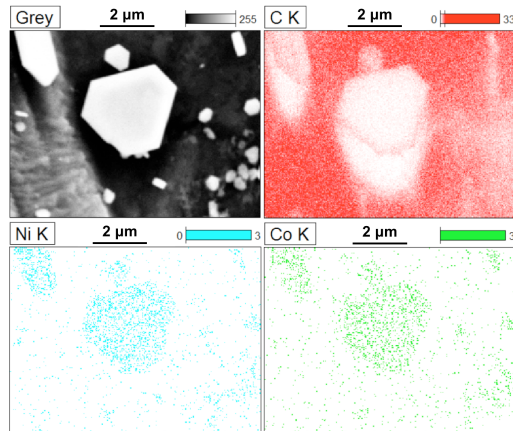


Figure S3. SEM image and EDS mapping micrographs of the NiCo LDH nanoplates made by a static hydrothermal reaction showing the distribution of Ni and Co elements.



Figure S4. Photograph of the colloidal emulsion of the exfoliated LDH powder sample showing light scattering upon irradiation with a laser beam.

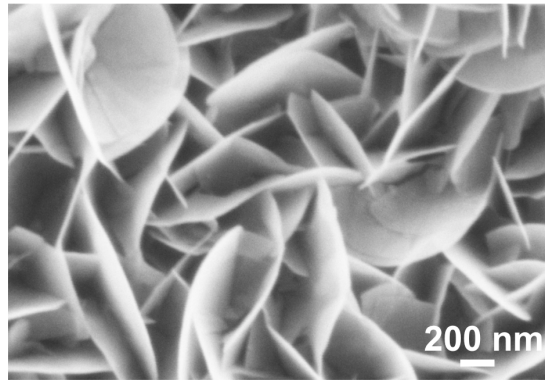


Figure S5. SEM image of the as-exfoliated NiCo LDH nanosheets.

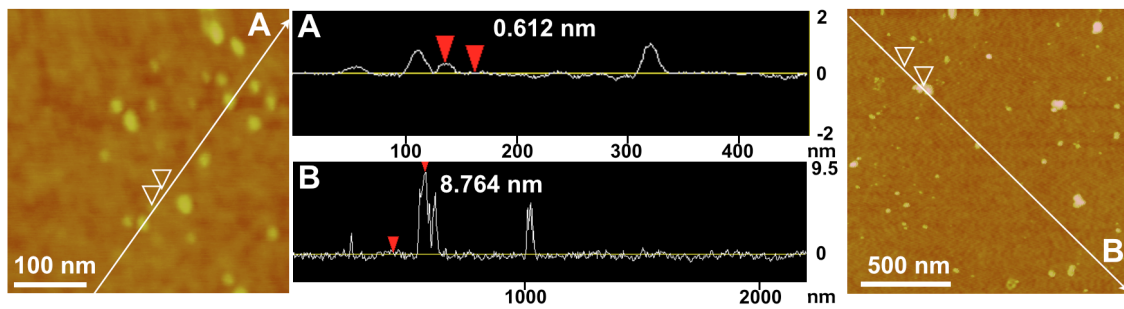


Figure S6. Tapping-mode AFM topographical images and corresponding height profiles of the exfoliated NiCo LDH nanosheets deposited on a silicon substrate.

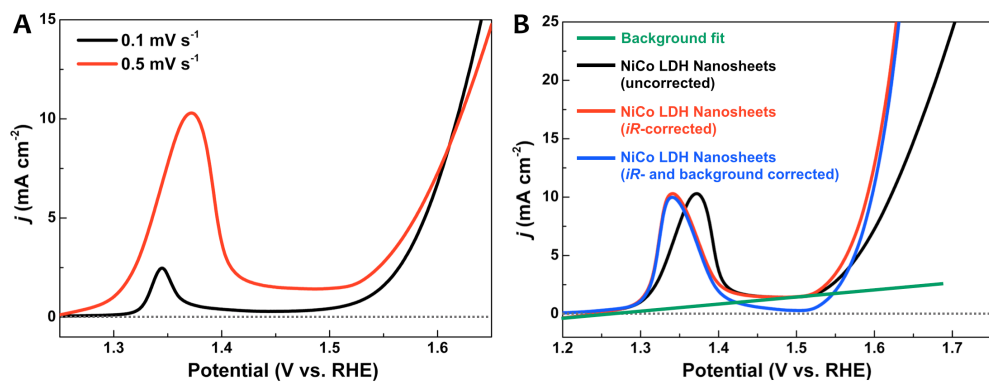


Figure S7. (A) Polarization curves of the exfoliated NiCo LDH nanosheets in O₂-saturated 1 M KOH at a scan rate of 0.1 (black curve) and 0.5 (red curve) mV s⁻¹. (B) Illustration of the method of *iR* and background correction that has been applied to all collected current density-voltage

measurements presented in Figure 4 of the main text (here the exfoliated NiCo LDH nanosheets are used as an example).

To fairly compare the catalytic activity of various NiCo LDH nanostructures, the polarization curves were corrected for all ohmic losses throughout the system using resistance extracted from the electrochemical impedance spectroscopy measurements. We also observed a substantial background (capacitive non-faradaic) current for the NiCo LDHs, particularly the exfoliated NiCo LDH nanosheets with high surface area. The background current is stable, and its magnitude is significantly increased at faster scan rates (Figure S5A). Its effect artificially shifts the polarization curves to higher current densities. Subtraction of this background current (Figure S5B) permits more clear and faithful analysis of the catalytic activity toward the faradaic process of interest (in this case, the OER). The data shown in Figure S5B without background correction gives $j = 10 \text{ mA cm}^{-2}$ at an overpotential (η) of 361 mV vs. RHE, while after background correction $j = 10 \text{ mA cm}^{-2}$ is observed at $\eta = 367 \text{ mV}$ vs. RHE. In spite of the relatively minor difference, proper data correction ensures that the catalytic performance is accurately and consistently represented.

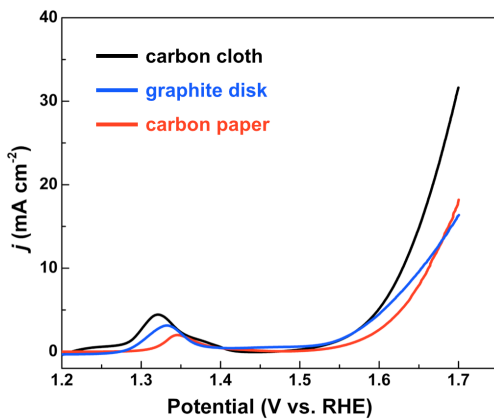


Figure S8. IR -corrected and background subtracted polarization curves of NiCo LDH grown on carbon paper, carbon cloth and graphite disk in O_2 -saturated 1 M KOH at a scan rate 0.5 mV s^{-1} . For the measurement of NiCo LDH nanoplates grown on graphite disk, the graphite disk was affixed to a glassy carbon rotating disk electrode (RDE) using graphite paint and then served as the working electrode. The working electrode was rotated at 1200 RPM during the measurement.

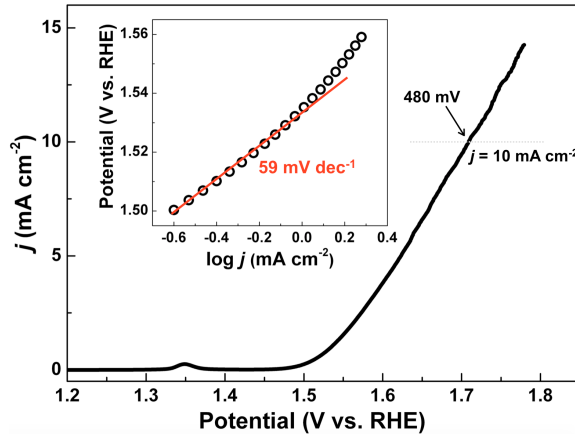


Figure S9. *IR*-corrected polarization curve of the NiCo LDH powder sample that was collected from the suspensions flowed through HCFR in O_2 -saturated 1 M KOH at a scan rate 0.5 mV s^{-1} and the corresponding Tafel slope (inset). For the electrode preparation, 6 mg NiCo LDH powder was mixed with polyvinylidene fluoride (PVDF) and N-methyl pyrrolidone (NMP), followed by sonication to form a homogeneous ink (the mass ratio of active material is 75%). Then the catalyst ink was loaded onto a carbon paper, which after being dried at 60°C for 30 min then served as the electrode (catalyst loading: 1.73 mg cm^{-2}). As shown in Figure S6, for such NiCo LDH powder sample, it requires an overpotential of 480 mV to achieve the significant O_2 evolution ($j = 10 \text{ mA cm}^{-2}$), which is 50 mV larger than that for the thin nanoplates directly grown on carbon paper made using HCFR with even much less catalyst loading.

Table S1. Comparison of catalytic performance of the exfoliated NiCo LDH nanosheets to other recently reported high performance OER catalysts.

Catalysts	Electrolyte	$\eta @ 1 \text{ mA cm}^{-2}$ (V)	$\eta @ 10 \text{ mA cm}^{-2}$ (V)	$j @ 300 \text{ mV}$ (mA cm^{-2})	Tafel slope (mV dec^{-1})	Ref.
NiCo LDH nanosheets	1 M KOH	0.302	0.367	0.683	40	This work
CoO_x^a	1 M KOH	0.381 ± 0.012	0.423 ± 0.013	0.020 ± 0.009	42 ± 1	S2
$\text{Co}_3\text{O}_4/\text{N-rmGO}^b$	1 M KOH	/	0.310	/	67	S3
CoO_x	1 M NaOH	/	0.390 ± 0.040	/	/	S4
NiO_x^a	1 M KOH	0.300 ± 0.003	/	1.01 ± 0.22	29 ± 0.4	S2
$\alpha\text{-Ni(OH)}_2$	0.1 M KOH	/	0.331	/	42	S5
$\beta\text{-Ni(OH)}_2$	0.1 M KOH	/	0.444	/	111	S5

Catalysts	Electrolyte	$\eta @ 1 \text{ mA cm}^{-2}$ (V)	$\eta @ 10 \text{ mA cm}^{-2}$ (V)	$j @ 300 \text{ mV}$ (mA cm ⁻²)	Tafel slope (mV dec ⁻¹)	Ref.
Ni _{0.25} Co _{0.75} O _x ^a	1 M KOH	0.341 ± 0.005	0.377 ± 0.006	0.079 ± 0.018	36 ± 1	S2
Ni _{0.5} Co _{0.5} O _x ^a	1 M KOH	0.320 ± 0.004	0.355 ± 0.006	0.30 ± 0.07	35 ± 2	S2
Ni _{0.75} Co _{0.25} O _x ^a	1 M KOH	0.312 ± 0.001	0.345 ± 0.002	0.47 ± 0.05	33 ± 1	S2
Ba _{0.5} Sr _{0.5} Co _{0.8} Fe _{0.2} O _{3-δ}	0.1 M KOH	≈ 0.314	≈ 0.362	/	≈ 48	S6
NiFe LDH/carbon nanotubes	1 M KOH	/	0.247	/	/	S7
ZnCo LDH ^c	0.1 M KOH	/	0.512 ~ 0.570	/	83~99	S8
CoNi LDH	0.1 M KH ₂ PO ₄	≈ 0.500	/	/	230 ~ 260	S9
NiCo LDH ^d	1 M KOH	0.292	0.334	1.533	41	S10
CoCo LDH ^d	1 M KOH	0.335	0.393	0.287	59	S10
P-doped graphitic C ₃ N ₄ ^e	0.1 M KOH	/	0.4	/	61.6	S11
graphitic C ₃ N ₄ nanosheets/carbon nanotubes	0.1 M KOH	/	0.37	/	83	S12
N and O dual-doped carbon hydrogel film	0.1 M KOH	/	/	/	141	S13
IrO ₂	1 M KOH	0.378 ± 0.004	0.427 ± 0.005	0.063 ± 0.036	49 ± 1	S2

Notes: ^aThin film. ^bNickel foam support. ^cNickel foil support. ^dSingle layer. ^eCarbon fiber paper support.

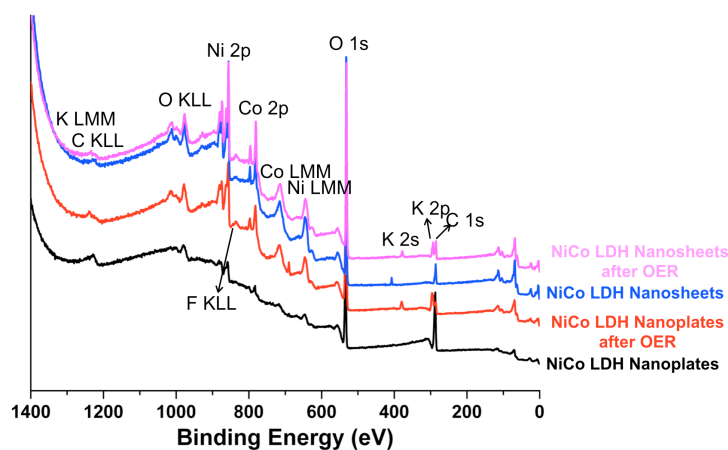


Figure S10. XPS survey spectra of the as-grown and exfoliated NiCo LDH nanostructures before and after OER tests.

References:

- (S1) Li, Y.; Y. Wu. *Chem. Mater.* **2010**, *22*, 5537-5542.
- (S2) Trotochaud, L.; Ranney, J. K.; Wiliams, K. N.; Boettcher, S. W. *J. Am. Chem. Soc.* **2012**, *134*, 17253-17261.
- (S3) Liang, Y.; Li, Y.; Wang, H.; Zhou, J.; Wang, J.; Regier, T.; Dai, H. *Nat. Mater.* **2011**, *10*, 780-786.
- (S4) McCrory, C. C. L.; Jung, S.; Peters, J. C.; Jaramillo, T. F. *J. Am. Chem. Soc.* **2013**, *135*, 16977-16987.
- (S5) Gao, M.; Sheng, W.; Zhuang, Z.; Fang, Q.; Gu, S.; Jiang, J.; Yan, Y. *J. Am. Chem. Soc.* **2014**, *136*, 7077-7084.
- (S6) Suntivich, J.; May, K. J.; Gasteiger, H. A.; Goodenough, J. B.; Shao-Horn, Y. *Science* **2011**, *334*, 1383-1385.
- (S7) Gong, M.; Li, Y.; Wang, H.; Liang, Y.; Wu, J. Z.; Zhou, J.; Wang, J.; Regier, T.; Wei, F.; Dai, H. *J. Am. Chem. Soc.* **2013**, *135*, 8452-8455.
- (S8) Li, Y.; Zhang, L.; Xiang, X.; Yan, D.; Li, F. *J. Mater. Chem. A* **2014**, *2*, 13250-13258.
- (S9) Zhang, Y.; Cui, B.; Zhao, C.; Lin, H.; Li, J. *Phys. Chem. Chem. Phys.* **2013**, *15*, 7363-7369.
- (S10) Song, F.; Hu, X. *Nat. Commun.* **2014**, *5*, 4477.
- (S11) Ma, T. Y.; Ran, J.; Dai, S.; Jaroniec, M.; Qiao, S. Z. *Angew. Chem., Int. Ed.* **2015**, doi: 10.1002/anie.201411125.
- (S12) Ma, T. Y.; Dai, S.; Jaroniec, M.; Qiao, S. Z. *Angew. Chem., Int. Ed.* **2014**, *53*, 7281-7285.
- (S13) Chen, S.; Duan, J.; Jaronies, M.; Qiao, S. Z. *Adv. Mater.* **2014**, *26*, 2925-2930.